scientific reports

OPEN

Effects of insertion of an h-AlN monolayer spacer in Pt-WSe_2-Pt field-effect transistors

Ken-Ming Lin[1], Po-Jiun Chen[1], Chih-Piao Chuu[3] & Yu-Chang Chen[1,2]✉

The growth of two-dimensional hexagonal aluminum nitride (h-AlN) on transition metal dichalcogenide (TMD) monolayers exhibits superior uniformity and smoothness compared to HfO_2 on silicon substrate. This makes an h-AlN monolayer an ideal spacer between the gate oxide material and the WSe_2 monolayer in a two-dimensional field effect transistor (FET). From first principles approaches, we calculate and compare the transmission functions and current densities of Pt–WSe_2–Pt nanojunctions without and with the insertion of an h-AlN monolayer as a spacer in the gate architecture. The inclusion of h-AlN can alter the characteristics of the Pt–WSe_2–Pt FET in response to the gate voltage (V_g). The FET without (or with) h-AlN exhibits the characteristics of a P-type (or bipolar) transistor: an on/off ratio of around 2.5×10^6 (or 1.7×10^6); and an average subthreshold swing (S.S.) of approximately 109 mV/$\mathrm{dec.}$ (or 112 mV/$\mathrm{dec.}$), respectively. We observe that V_g shifts the profile of the transmission function by an energy of $\alpha(eV_g)$, where α represents the gate-controlling efficiency. We observed that $\alpha_{in} = 83\%$ and $\alpha_{out} = 33\%$, corresponding to whether the Fermi energy is located inside or outside the band gap. Therefore, we construct an effective gate model based on the Landauer formula, with the transmission function at $V_g = 0$ as the baseline. Our model generates results that are consistent with those obtained through first principles calculations. The relative error in current densities between model and first-principles calculations is within $[\frac{ln(10)}{S.S.}]|\Delta V_G^{eff}|$. The 2D atomistic FETs show excellent device specifications and the ability to compete with existing transistors based on traditional silicon technology. Our findings could help advance the design of TMD-based FETs.

Keywords Density functional theory, Non-equilibrium Green's function, 2D field effect transistor, Subthreshold swing

The miniaturization of Field-Effect Transistors (FETs) allows for the incorporation of a large number of transistors into a single chip, resulting in high-density integration[1]. High density packing of transistors improves the performance of the chip and lowers the joule heating, which makes the use of energy more efficient. The process of reducing the size of FETs encourages the advancement of nanotechnology. Two-dimensional materials Monolayer, such as Transition Metal Dichalcogenides (TMDs), are a promising emerging choice for the channel material in the next-generation Field-Effect Transistors. Transition metal dichalcogenides are a class of ultrathin semiconductors consisting of atomic layers. They exhibit ideal band gaps, surfaces free of dangling bonds, high mobilities, and low subthreshold swings. However, the contact resistance due to the Schottky barrier in contacts between transition TMDs and metal leads is significantly higher when compared to metal-silicon contacts[2]. A critical challenge for 2D-TMD FETs to compete with traditional silicon-based FETs is to reduce the contact resistance. Several research groups have postulated that employing metals with varying work functions could potentially reduce the height of the Schottky barrier in contacts[3–6]. Kang et al. employed Density-Functional Theory (DFT) calculations to simulate the contact between metal and TMDs using both edge and top contacts. The edge contacts offer significant advantages over the top contact in terms of electron injection efficiency[7]. Several experimental findings have demonstrated that TMDs undergo a phase transition from semiconducting to metallic under stress or external irradiation[8–11]. Moreover, Jiang and Kappera proposed that using an ultrathin layer of MoS_2 with metallic 1T-phase contact in a field-effect transistor (FET) can greatly decrease the contact resistance between the source/drain electrodes and subthreshold swing[12,13]. Recent theoretical calculations and experiments have revealed that Platinum Dichalcogenides (PD) exhibit a thickness-dependent electronic structure[14,15]. Monolayer PD is shown to be a type of semiconductor. Few layers of PD, on the other hand,

[1]Department of Electrophysics, National Yang Ming Chiao Tung University, 1001 University Road, Hsinchu City 300093, Taiwan. [2]Center for Theoretical and Computational Physics, National Yang Ming Chiao Tung University, 1001 University Road, Hsinchu City 300093, Taiwan. [3]Taiwan Semiconductor Manufacturing Company (TSMC), Hsinchu 30010, Taiwan. ✉email: yuchangchen@nycu.edu.tw

show metallic properties. Through the use of DFT in conjunction with non-equilibrium Green's function (NEGF), AlMutairi and Yang proposed that the lateral heterostructure of monolayer metallic and multilayer semicoducting $PtSe_2$ can offer a lower contact resistance[16,17]. In 2021, Shen and Chou observed that there is an extremely low resistance to electrical contact, specifically a Schottky barrier height of zero and ohmic contact, at the interface between the semi-metallic bismuth/antimony and the semiconducting monolayer MoS_2. This is due to a lower Density of States (DOS) near the Fermi energy. Consequently, there are fewer metal-induced gap states and less charge transfer at the interface between the semimetal and MoS_2[18,19]. Two dimensional MSi_2M_4 (M = Nb, Ta, Mo, W) heterojunctions exhibit P-type transistors behavior and possess subthreshold swings that can surpass the limit of Boltzmann's tyranny, 60 mV/dec. at room temperature[20]. Theoretical calculations suggest that bismuth employed as electrodes with reduced contact resistance may exceed the classical limit of thermionic current[21].

Fang and colleagues conducted an experiment where they observed that exposing the contact region of a WSe_2 monolayer field-effect transistor (FET) to NO_2 resulted in chemically doping. The introduction of chemically doped contacts resulted in a decrease in contact resistance, transforming the device into a high-performance P-type field-effect transistor[22]. To reduce contact resistance, a mild H_2 plasma treatment can be used to induce anion (Se) vacancies in the WSe_2 lattice at the contact regions[23]. Meanwhile, Jiang and colleagues reported that a nitrogen plasma induces the formation of sulfur vacancies in tungsten disulfide nanoflakes, followed by the doping of nitrogen atoms onto these vacancies[24]. Chung employed the first-principles method to evaluate the performance of WS_2 and platinum electrodes by introducing group V atoms at the interface. The researchers discovered that the contact resistance for the P-type contacts decreased from approximately 300 $\Omega\ \mu\mathrm{m}$ to less than 150 $\Omega\ \mu\mathrm{m}$.[25]

Experimental physicists manipulate contact regions to create vacancies or add impurities in order to enhance contact resistance. Additionally, they incorporate insertion layers to improve the performance of transport properties. For instance, in a study conducted by Iqbal et al. 2015, it was demonstrated that a monolayer-WS_2 FET sandwiched between chemical vapor deposition-grown Boron Nitride film displayed a high level of electron mobility as a property of its transport at room temperature[26]. Hu's group demonstrated the growth of two-dimensional Hexagonal Aluminum Nitride (h-AlN) on transition metal dichalcogenide (TMD) monolayers, such as MoS_2, WS_2, and WSe_2, using van der Waals epitaxy through Atomic Layer Deposition (ALD). In such case, the AlN film displayed a two-dimensional layered structure on TMDs[27]. The AlN film exhibits superior uniformity and smoothness compared to HfO_2, making it an excellent option for the gate dielectric interfacial layer in TMD transistors.

While numerous authors have explored various techniques to enhance transport properties, there is currently no literature available on the investigation of the gating effects of h-AlN as an insulating 2D spacer between the TMD channel and the gate. From fist-principles approaches, this paper presents a comparison of the current density in response to the gate voltage for short channel Pt–WSe_2–Pt transistors. The transistors are illustrated in Fig. 1 and consist of structures with and without an h-AlN layer serving as spacer layers between the single-layered WSe_2 channel and the gate oxide. Our calculations demonstrate that the primary factor influencing the effectiveness of the gate control is the geometric structure of the gate oxide, regardless of the insertion of h-AlN layers. The first-principles computations show that the transmission function's shapes are not significantly altered by the gate voltages. The principal consequence of the applied gate voltages is to shift the location of the chemical potential with respect to the edges of the band gap. This enables us to define a gate controlling efficiency, which characterizes the efficiency to shift the location of the chemical potential with respect to the boundaries of the band gap. We find that when the chemical potentials are between the band gap, the gate controlling efficiency is about 83$\%$. On the other hand, when the gate voltage, V_g, moves the chemical potentials out of the band gap, the gate controlling efficiency drops to roughly 33$\%$. These characteristics enable us to build an efficient model with the Landauer formula, which merely uses the information of transmission function at $V_\mathrm{g}=0$ to illustrate how the gate voltage modulates the current density.

Theory

VASP

The Perdew–Burke–Ernzerhof functional (PBE)[28–31], a type of Generalized Gradient Approximation (GGA) used to account for the many-body effects in the independent particle picture of the auxiliary Kohn-Sham system, was employed in the Density Functional Theory (DFT) analysis. We utilized the precise full-potential projected augmented wave method with the plane-wave basis, implemented in the Vienna Ab-initio Simulation Package (VASP), to solve the Kohn-Sham equation[32–35]. For all of our DFT calculations, we utilized a grid size of 0.016 Å^{-1} in reciprocal space and a plane-wave energy cutoff of 400 eV. The termination condition for the electronic self-consistent iterations was set at 1.0×10^{-4} eV. In addition, a Gaussian smearing technique was employed with a smearing factor of 25 meV to replicate the Density of States (DOS) from $\Sigma_{n,\vec{k},\sigma}\ \delta(E - E_{n,\sigma}(\vec{k}))$

, which involves the quantum numbers such as the band index n, crystal momentum $\vec{k}$, and spin index σ. This was done to determine the energies of the valence band maximum or the conduction band minimum, and the Fermi energy.

Nanodcal

Nanodcal (Nanoacademic device calculator) is designed for quantitative modeling of quantum transport at the atomic level. The nanodcal program requires the spatial positions of the atoms, the structure of gate, and the applied source-drain bias that make up the nanostructure as inputs. NanoDCAL performs self-consistent calculations based on the Keldysh nonequilibrium Green's function with the linear combination of atomic orbitals (LCAO) implemented in the density functional theory (DFT)[36–38]. In 2D TMD transistors with short

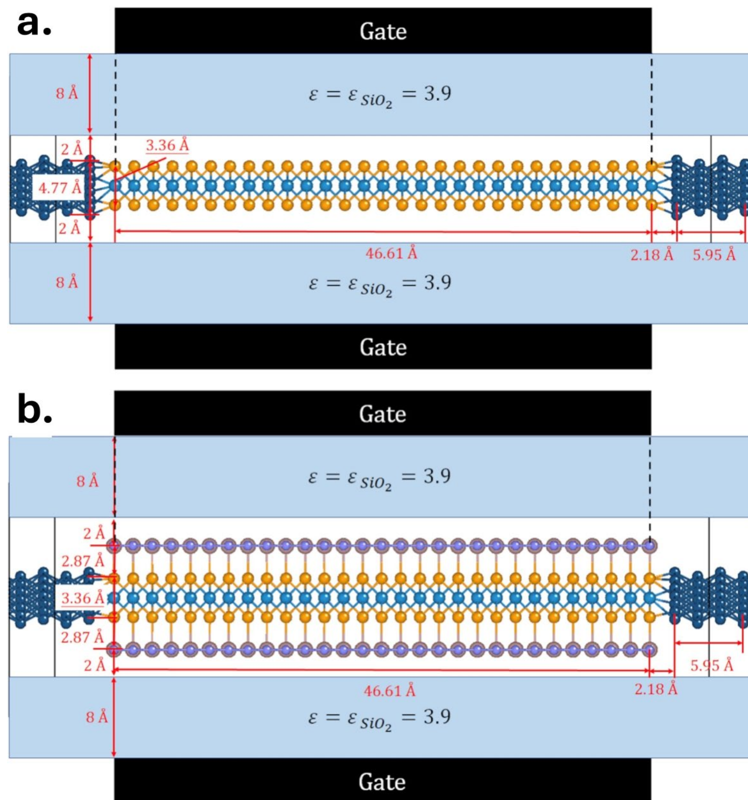

Fig. 1. Schematics of Pt–WSe_2–Pt field effect transistors without and with h-AlN. The side views of the Pt–WSe_2–Pt transistors are depicted in (**a**) without and (**b**) with a monolayer of h-AlN acting as the insulating spacer between the gate and the WSe_2 2D channel. The length of the channel is 46.61 Å. The gate's equivalent oxide thickness (EOT) is represented by a dielectric material with a relative permittivity of 3.9 and a thickness of 8 Å.

channels, as shown in Fig. 1, the length of the channel is smaller than the average distance an electron can travel without scattering, resulting in the current being in the quantum transport region[39]. Hence, the transmission functions, $\tau(E)$, are computed using Nanodcal which takes into account the source-drain voltage V_{ds} and the gate voltage V_{g}.

The one-body Green's function can be defined by $(E - H)G(E) = \mathbf{1}$[40]. For a two-probes system, H can be separated into the left-lead (H_{L}), right-lead (H_{R}) and center region (H_{C}) as,

$$H = \begin{pmatrix} H_{\mathrm{L}} & \tau_{\mathrm{L}} & 0 \\ \tau_{\mathrm{L}}^{+} & H_{\mathrm{C}} & \tau_{\mathrm{R}}^{+} \\ 0 & \tau_{\mathrm{R}} & H_{\mathrm{R}} \end{pmatrix}, \tag{1}$$

where $\tau_{\mathrm{L,R}}$ describes the interaction between left/right-lead and center region.

Using Eq. (1) and Green's function definition, one obtains:

$$\begin{pmatrix} E - H_{\mathrm{L}} & \tau_{\mathrm{L}} & 0 \\ \tau_{\mathrm{L}}^{+} & E - H_{\mathrm{C}} & \tau_{\mathrm{R}}^{+} \\ 0 & \tau_{\mathrm{R}} & E - H_{\mathrm{R}} \end{pmatrix} \begin{pmatrix} G_{\mathrm{L}} & G_{\mathrm{LC}} & G_{\mathrm{LR}} \\ G_{\mathrm{CL}} & G_{\mathrm{C}} & G_{\mathrm{CR}} \\ G_{\mathrm{RL}} & G_{\mathrm{RC}} & G_{\mathrm{R}} \end{pmatrix} = \mathbf{1}. \tag{2}$$

The G_{C} is the sub-matrix of the full Green's function G for the central region and have a form of $G_{\mathrm{C}} = (E - H_{\mathrm{C}} - \Sigma_{\mathrm{L}} - \Sigma_{\mathrm{R}})^{-1}$. where $\Sigma_{\mathrm{L}} = \tau_{\mathrm{L}}^{+} G_{\mathrm{L}} \tau_{\mathrm{L}}$ and $\Sigma_{\mathrm{R}} = \tau_{\mathrm{R}}^{+} G_{\mathrm{R}} \tau_{\mathrm{R}}$ are the self-energies. The $G_{\mathrm{L,R}}$ are the Green's function of the leads, which satisfies the definition of the single particle Green's function, i.e., $G_{\mathrm{L,R}} = (E - H_{\mathrm{L,R}})^{-1}$. Since the $H_{\mathrm{C}} + \Sigma_{\mathrm{L}} + \Sigma_{\mathrm{R}}$ in the Eq. (3) is a non-Hermition Hamiltonian for an open system, the eigenvalues could be complex numbers. The imaginary component of the self-energies causes the eigen-energies to broaden. The linewidth or broadening function $\Gamma_{\mathrm{L,R}}$ was determined by $\Gamma_{\mathrm{L,R}} = i(\Sigma_{\mathrm{L,R}} - \Sigma_{\mathrm{L,R}}^{+})$.

The total current calculated in the Nanodcal package is

$$I_{\mathrm{N}} = I_{\mathrm{R}} - I_{\mathrm{L}}, \tag{3}$$

where $I_{\mathrm{L,R}} = \frac{e}{\hbar}\int_{-\infty}^{\infty}\frac{dE}{2\pi}\tilde{I}_{L,R}(E)$. Note that $\tilde{I}_{\mathrm{L,R}} = \mathrm{Tr}(\Gamma_{\mathrm{L,R}}A)f_{\mathrm{L}} - \mathrm{Tr}(\Gamma_{\mathrm{L,R}}G^n)$. The total spectral function $A = A_{\mathrm{L}} + A_{\mathrm{R}}$ comes from left and right spectral functions, $A_{\mathrm{L,R}} = G_{\mathrm{C}}\Gamma_{\mathrm{L,R}}G_{\mathrm{C}}^{+}$. The partial spectral function G^n is $G^n = A_{\mathrm{L}}f_{\mathrm{L}} + A_{\mathrm{R}}f_{\mathrm{R}}$.

The following numerical parameters are used in the Nanodcal quantum transport calculations. Troullier-Martins norm-conserving pseudopotentials were used to simulate electron-ionic core interactions[41]. Double-ζ polarized basis sets were used to treat elemental valence electrons. PBE-GGA was chosen as the exchange-correlation functional[31,42]. The equivalent energy cut-off of the grid density was set to be 100 Hartree. The Brillouin zone of the reciprocal space was sampled using a grid of dimensions $6 \times 1 \times 100$ for the electrodes and $6 \times 1 \times 1$ for the central scattering region. The number of *k*-points used to calculate the transmission coefficient and current are $6 \times 1 \times 1$ and $1 \times 1 \times 100$ respectively.

Figure 1a,b depict the two different configurations of Pt–WSe_2–Pt FETs, one without h-AlN and the other with a monolayer of h-AlN. The channel length of monolayer tungsten diselenide (WSe_2) is 46.61 Å, and the double gates were designed to have the same length. The thickness between top and bottom gates is around 24 Å. The gate's insulator is considered to be made of Silicon Dioxide (SiO_2). Its equivalent oxide thickness (EOT) is 8 Å, and its relative permittivity is 3.9. Using VASP, the lattice constant of monolayer tungsten diselenide (WSe_2) was optimized to 3.331 Å. The lattice constant matches what has been found in previous DFT studies (3.329 Åand in experiments (3.280 Å) [43,44]. Specifically, because of its P-type FET properties, we chose face-centered cubic platinum as the metal lead with a theoretical lattice constant of 2.755 Å[45]. The Miller index of the platinum electrodes is chosen to minimize the lattice mismatch to 0.33% at the interface between the WSe_2 and Pt electrodes. To avoid lattice mismatch in the simulation box, an isotropic compress strain was applied to the platinum leads. We used the energy minimization method to determine the distances (2.18 Å) between the platinum surface and WSe_2 for the edge contact. The monolayer h-AlN was taken into consideration in this computation as the AlN thin film changed from a 3D to a 2D crystal structure [27]. Monolayer AlN was subjected to a compressed strain in order to achieve a lattice match with the WSe_2. The inter-layer distance between the h-AlN and WSe_2 monolayer was relaxed to 2.87 Å using the energy minimization method. During the energy minimization process, the van der Waals force was incorporated into the DFT calculation using the Grimme DFT-D2 method. The Ref. [46] is included[46]. In addition, the aluminum atom in h-AlN locates on the top of the center of the hexagonal WSe_2 , resulting in the lowest total energy.

In this first-principles calculations, the temperature is maintained at $T = 300$ K and the drain-source voltage is fixed at $V_{\mathrm{ds}} = 50$ mV. The current computed using Eq. (3) in Nanodcal can be casted into the Landauer formula[47–49],

$$I_{\mathrm{N}}(V_{\mathrm{g}}) = \frac{2e}{h}\int_{-\infty}^{\infty}\left(f_{\mathrm{L}} - f_{\mathrm{R}}\right)\tau(E;V_{\mathrm{g}})\,dE, \tag{4}$$

where the transmission function $\tau(E;V_{\mathrm{g}})$ is a function of V_{g}. The Fermi-Dirac distributions, respectively, in the left and right leads are

$$f_{\mathrm{R}}(E,T) = \frac{1}{e^{[E-(\mu)]/k_{\mathrm{B}}T}+1}, \tag{5}$$

and

$$f_{\mathrm{L}}(E,T) = \frac{1}{e^{[E-(\mu-eV_{\mathrm{ds}})]/k_{\mathrm{B}}T}+1}, \tag{6}$$

where k_{B} is the Boltzmann constant, and T is the temperature. Here, we've assumed that the right lead is grounded, with *mu* representing its chemical potential. The left lead's chemical potential shifts from μ to $(\mu - eV_{ds})$ upon the application of the source-drain bias V$_{ds}$. Note that $(f_{\mathrm{L}} - f_{\mathrm{R}})$ opens an energy window formed between $(\mu - eV_{ds})$ and μ for the tunneling electrons. The energy widows, broadened by a few k_BT due to the temperature, are the primary source of tunneling electrons for the current $I_{\mathrm{N}}(V_{\mathrm{g}})$.

Model of effective-gate voltage for the current

The electronic structures (or transmission functions) of the junction are shifted by the application of the gate voltage, V_{g}, by an energy of $eV_{\mathrm{G}}^{\mathrm{eff}}(V_g)$ relative to the chemical potential, which is used as the reference energy. Alternatively, if we consider the transmission function at $V_{\mathrm{g}} = 0$, denoted as $\tau(E;V_{\mathrm{g}} = 0)$, as the baseline, the impact of applying a gate voltage V_{g} is to displace the chemical potential E_F to $[E_F + eV_{\mathrm{G}}^{\mathrm{eff}}(V_g)]$. In this scenario, the current, $I_{\mathrm{M}}[V_{\mathrm{G}}^{\mathrm{eff}}]$, can be calculated by using $\tau(E;V_{\mathrm{g}} = 0)$ as the baseline,

$$I_{\mathrm{M}}[V_{\mathrm{G}}^{\mathrm{eff}}(V_g)] = \frac{2e}{h}\int_{-\infty}^{\infty}\left(f_{\mathrm{L}}^{\mathrm{M}} - f_{\mathrm{R}}^{\mathrm{M}}\right)\tau(E;V_{\mathrm{g}} = 0)\,dE, \tag{7}$$

where the chemical potentials in the left and right leads are shifted by the application of the gate voltage V_{g} by an energy of $eV_{\mathrm{G}}^{\mathrm{eff}}(V_g)$ in the Fermi-Dirac distributions,

$$f_{\mathrm{R}}^{\mathrm{M}}[E,T,V_{\mathrm{G}}^{\mathrm{eff}}(V_{\mathrm{g}})]=\frac{1}{e^{[E-(\mu+eV_{\mathrm{G}}^{\mathrm{eff}}(V_g))]/k_{\mathrm{B}}T}+1}, \tag{8}$$

and

$$f_{\mathrm{L}}^{\mathrm{M}}[E,T,V_{\mathrm{G}}^{\mathrm{eff}}(V_{\mathrm{g}})]=\frac{1}{e^{[E-(\mu-eV_{ds}+eV_{\mathrm{G}}^{\mathrm{eff}}(V_g))]/k_{\mathrm{B}}T}+1}, \tag{9}$$

respectively. The currents I_{N} and I_{M} (Eqs. 4 and 7) divided by the width of the TMD channel located within the simulation box yield the current densities J_{N} and J_{M}, respectively.

The subthreshold swing (S.S.) of a transistor is a measure of its efficiency to be turned on or off the current. For J_{N} and J_{M}, the subthreshold swings are defined as,

$$S.S.(\mathrm{N/M})\equiv\left\{\frac{d\log_{10}\left[J_{\mathrm{N/M}}\left(V_g\right)\right]}{dV_g}\right\}^{-1}, \tag{10}$$

which depicts the amount of gate voltage that needs to be changed in order to raise the output current by a decade.

Computing the current I_{N} using Eq. (3) from first-principles approaches demands significant computational resources. For each specific T, V_{g} and V_{ds}, self-consistent calculations in DFT+NEGF are performed in the Nanodcal package to obtain the current. In sharp contrast, computing the current density J_{M} using the model of effective gate using Eq. (7) can reduce significant amount of computational power. Motivated by the above mentioned reason, we build a models of effective gate voltage $V_{\mathrm{G}}^{\mathrm{eff(M)}}(V_{\mathrm{g}})$ [c.f. Eqs. (12) and (13)] to calculate $J_{\mathrm{M}}[V_{\mathrm{G}}^{\mathrm{eff(M)}}(V_{\mathrm{g}})]$ base on observations from results of first-principles calculations. The calculations take the transmission function at zero gate voltage, $\tau(E;V_{\mathrm{g}}=0)$, as the baseline. For each specific T, V_{g} and V_{ds}, the model of effective gate can be applied to calculate the current, and thus can save a lot of time and significant computational resources to explore the gate-dependent and temperature dependent properties for the TMD nanojunction.

We illustrate that the discrepancy between J_{N} and J_{M} can be estimated by using the information of the subthreshold swing:

$$\left|\frac{\Delta J}{J_{\mathrm{N}}}\right|\approx ln(10)\cdot\left|\Delta V_{\mathrm{G}}^{\mathrm{eff}}\right|/(S.S.), \tag{11}$$

where $(\Delta J/J_{\mathrm{N}})\times 100\%$ is the percentage error between J_{N} and J_{M}, and $\Delta V_G^{\mathrm{eff}}\equiv|V_G^{\mathrm{eff(N)}}-V_G^{\mathrm{eff(M)}}|$ as illustrated in the discussion section.

Results and discussion

The side views of the Pt–WSe_2–Pt transistors are depicted in Fig. 1a without and b with a monolayer of h-AlN acting as the insulating spacer between the gate and the WSe_2 2D channel. The length of the channel is 46.61 Å. The gate's equivalent oxide thickness (EOT) is represented by a dielectric material with a relative permittivity of 3.9 and a thickness of 8 Å.

The atomic arrangement of a bulk AlN exhibits a three-dimensional Wurtzite structure. When a few layers of AlN are added on top of the monolayer WSe_2, we can observe through structure optimization using VASP that AlN undergoes a structural transition from the Wurtzite structure to h-AlN, which is a layered two-dimensional hexagonal structure. Figure 2a displays the band structures, density of states (DOS), and projected DOS (PDOS) of the pristine monolayer WSe_2. This is contrasted with Fig. 2b–d, which illustrate the density of states (DOS) and projected DOS (PDOS) for one to three layers of h-AlN on top of the monolayer WSe_2. The WSe_2 monolayer and the h-AlN multi-layers stacked on top of the WSe_2 monolayer both demonstrate semiconductor characteristics. The WSe_2 monolayer has a band gap of 1.45 eV. When a single layer, two layers, and three layers of h-AlN are deposited on the monolayer WSe_2, the resulting band gaps are 1.14, 1.23, and 1.13 eV, respectively. The Fermi energy, located at the midpoint of the band gap, coincides with the chemical potential of an intrinsic semiconductor at room temperature. This occurs because the electron number density in the conduction bands is equal to the hole number density in the valence bands [50].

The top panel of Fig. 3 displays four potential arrangements of a bilayer structure consisting of a single layer of h-AlN and a single layer of WSe_2. Based on first principles calculations using VASP, it has been determined that configuration (2) exhibits the highest stability and the lowest total energy. Figure 3a,b show the color map representing the projection of the band structures of the stable bilayer on h-AlN and WSe_2. The green color in Fig. 3a,b represents the weighting of the band structures contributed by h-AlN and WSe_2, respectively. It is evident that the valence band edge hybridizes as a result of the interaction between WSe_2 and h-AlN. The h-AlN monolayer dominates the states in the valence band, while the WSe_2 single layer has a lesser contribution. However, it is WSe_2 that primarily determines the conduction band edge, suggesting that h-AlN has a wider band gap and is therefore an insulator.

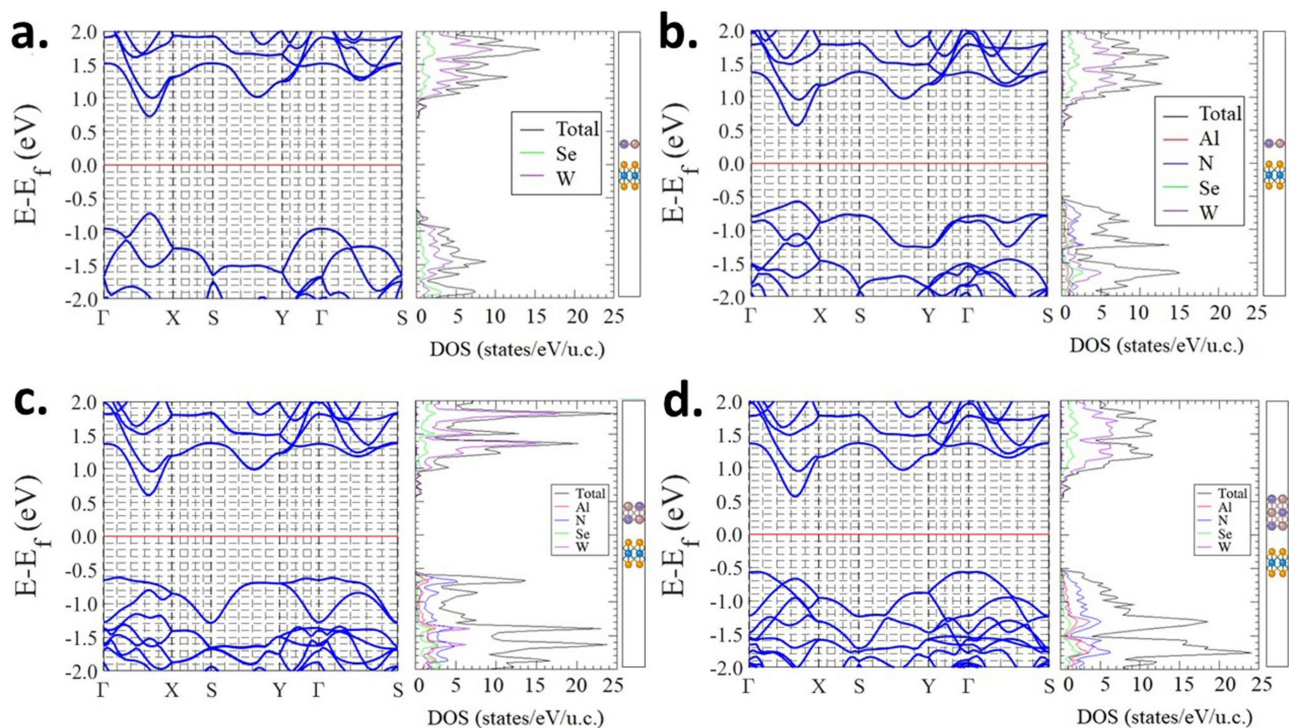

Fig. 2. Band structures of a monolayer WSe_2 and layers of h-AlN epitaxied on WSe_2. The left panel displays the band structures, while the right panel shows the density of states (DOS) and projected density of states (PDOS) for the following systems: (**a**) monolayer WSe_2; (**b**) single layer of hexagonal aluminum nitride (h-AlN); (**c**) two layers of h-AlN; and (**d**) three layers of h-AlN stacked on top of the monolayer WSe_2. The right panels exhibit the DOS represented by a black line, while the PDOS is projected onto Se, W, Al, and N atoms and depicted by green, purple, red, and blue lines, respectively. The paths of k-point paths are along the high symmetric points of the 2D Brillouin zone rectangular lattice (p2mm). The Se, W, Al, and N atoms are depicted as solid balls of orange, blue, pink, and purple color respectively. Band structures, DOS, and PDOS are plotted relative to the Fermi energy, which is defined as zero.

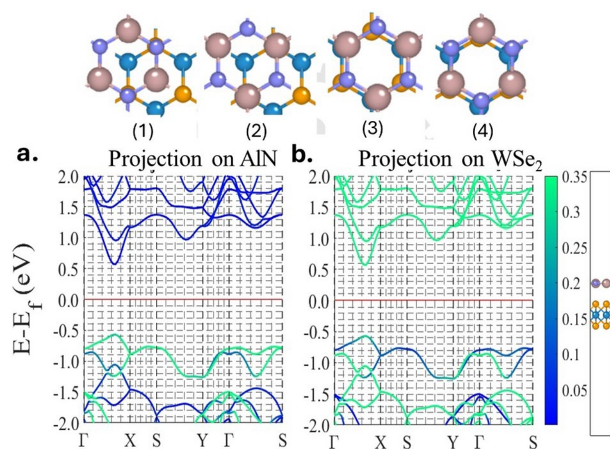

Fig. 3. Projected DOSs of a single layer of h-AlN epitaxied on WSe_2. The upper panel exhibits four possible configurations of a bilayer structure comprising a solitary layer of h-AlN and a solitary layer of WSe_2. The aluminum atoms positioned on the hollow site of $WeSe_2$ exhibit the lowest energy and form a stable structure, as shown in Configuration (2). The band structures' relative contributions from a single layer of (**a**) h-AlN and (**b**) WSe_2 are visually indicated by the color green. The Γ-X direction corresponds to the direction of the current and the directions of the zigzag edge. The Se, W, Al, and N atoms are depicted as solid balls of orange, blue, pink, and purple color respectively. Band structures are plotted relative to the Fermi energy, which is defined as zero.

The stable configurations depicted in Fig. 3 are dissected and linked to the Pt electrodes in order to establish the channel of the Pt–WSe_2–Pt transistors, as illustrated in Fig. 1a,b. The Nanodcal simulation package is utilized to compute the transmission functions for various gate voltages V_g, where the drain-source voltage V_{ds} is set to -50 mV. Figure 4a display the transmission functions $\tau(E; V_g)$ in the Pt–WSe_2–Pt transistors without h-AlN, when V_g ranging from $V_g = -0.7$ to 1.0 V is applied. Figure 4b presents the transmission function $\tau(E; V_g)$ with the h-AlN as an insulating spacer for different gate voltages ranging from $V_g = -1.2$ to 0.7 V. The energy profile of the transmission function clearly shows a band gap range, indicating that the Pt–WSe_2–Pt junction functions as a semiconductor tunneling field-effect transistor. In this transistor, the channel length is shorter than the average distance an electron travels before interacting with phonons. The transmission function has a significantly low magnitude for electrons with energy situated within the band gap region. This feature enables the tunneling transistor to effectively halt the flow of current with minimal leakage current. Our observation on Fig. 4 show that the energy profile of $\tau(E; V_g)$ is simply displaced an energy of $eV_G^{\rm eff}(V_g)$ with respect to $\tau(E; V_g = 0)$ by the application gate voltage V_g. As a result, we can use $\tau(E, V_g = 0)$ as the reference to create an effective gate model for $V_G^{\rm eff}(V_g)$.

Firstly, We determine the valence and conduction band edge, denoted as $E_V(V_g)$ and $E_C(V_g)$, respectively, for each value of V_g, by analyzing the second derivative of the transmission function $\tau(E; V_g)$. This analysis is shown in the top and middle panels in Fig. 5a,b, specifically for $V_g = 0$. We can see the transmission functions $\tau(E; V_g = 0)$ in linear and logarithmic scales for the Pt–WSe_2–Pt nanojunctions without and with the h-AlN single layer inserted into the gate architecture. The second derivative of $\tau(E; V_g = 0)$ with respect to E highlights the band gap regime formed between $E_V(V_g = 0)$ and $E_C(V_g = 0)$, as shown in the middle panels of Fig. 5a,b. The color bars represents the band gaps determined by the transmission functions. The graphs indicate that the Pt–WSe_2–Pt configuration without AlN exhibits P-type transistor behavior, with a band gap of approximately 1.55 eV. On the other hand, the Pt–WSe_2–Pt configuration with h-AlN demonstrates bipolar transistor characteristics, with a band gap of around 1.06 eV.

Using the chemical potential μ as the reference energy, the top panels of Fig. 6a,b illustrate the energy shifts of the band gaps of the transmission functions caused by the application of the gate voltage V_g. It demonstrates that when the chemical potential is within the band gap regime, the energy shifts of transmission functions are more effective. The energy shifts become less effective when the chemical potential move outside of the band gap regime. Shifting the band gaps of the transmission profiles by using the chemical potential μ as a reference when a gate voltage is applied is equivalent to shifting the chemical potentials using the transmission function at $V_g = 0$ as a reference. Thus, we can define the effective gate voltage as $V_G^{\rm eff(N)}(V_g) \equiv [E_V(V_g = 0) - E_V(V_g)]/e$

, using results obtained from first-principles calculations using Nanodcal. The energy shift of the chemical potential caused by the application of the gate voltage V_g is represented by $eV_G^{\rm eff(N)}(V_g)$. Figure 6a,b display $eV_G^{\rm eff(N)}(V_g)$ (blue solid circles) as a function of the gate voltage V_g in their lower panels. The slope for the $eV_G^{\rm eff(N)}$ vs. V_g represents the efficiency of gate controlling. It is fascinating to observe that the gate controlling efficiency

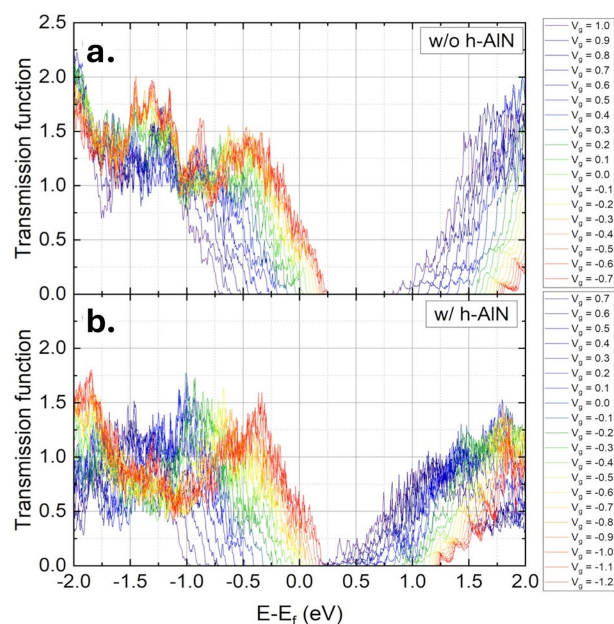

Fig. 4. Transmission functions obtained from Nanodcal. Panels (**a**) and (**b**) display the transmission functions of the Pt–WSe_2–Pt transistors without and with the inclusion of a single layer of h-AlN at various gate voltages (V_g) as a function of energy E, respectively. The drain-source bias voltage V_{ds} is set to -50 mV and the temperature is kept at 300 K. The reference energy for transmission functions at various applied V_g is the Fermi energy E_F when $V_g = 0$.

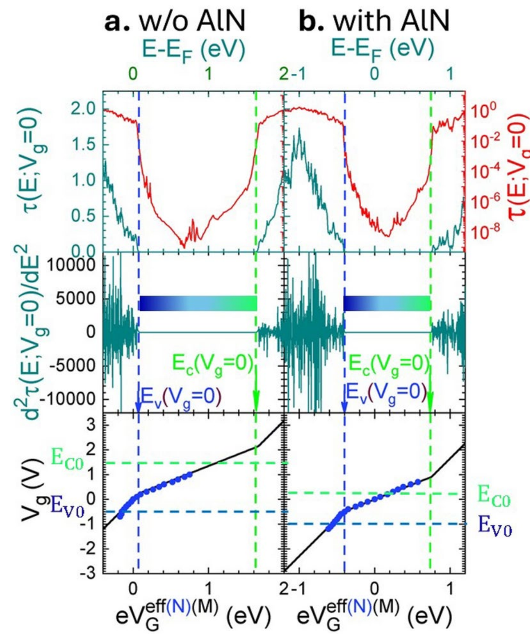

Fig. 5. Band gap of the transmission function and the position of chemical potential shifted by $V_{\mathrm{G}}^{\mathrm{eff}}$. The top panels display the transmission functions $\tau(E, V_{\mathrm{g}}=0)$ as a function of $E-E_F$ at $V_{\mathrm{g}}=0$ for the Pt–WSe_2–Pt transistors (**a**) without and (**b**) with h-AlN, respectively. The left axis corresponds to a linear scale (green solid line), while the right axis (red solid line) corresponds to a logarithmic scale; The middle panels display the second derivative of $\tau(E, V_{\mathrm{g}}=0)$ as a function of $E-E_F$ for the Pt–WSe_2–Pt transistors (**a**) without and (**b**) with h-AlN, respectively; The positions of the band gap boundaries, $E_{\mathrm{V}}(V_{\mathrm{g}}=0)$ (blue arrow) and $E_{\mathrm{C}}(V_{\mathrm{g}}=0)$ (green arrow), are also indicated by vertical dashed lines; The bottom panels show the gate voltage V_{g} (vertical axis) v.s. $eV_{\mathrm{G}}^{\mathrm{eff(N)}}$ (blue solid circles) or $eV_{\mathrm{G}}^{\mathrm{eff(M)}}$ (black solid line) for the Pt–WSe_2–Pt transistors (**a**) without and (**b**) with h-AlN, respectively.

is approximately 0.83 when the chemical potential is within the band gap. When the chemical potential is located outside the band gap, the gate controlling efficiency is reduced to approximately 0.33 due to the screening effect caused by the more conductive FETs. The gate controlling efficiencies are solely determined by the gate architecture and are not affected by the presence or absence of the h-AlN single layer. One possible explanation is that h-AlN is an insulator and does not have the ability to block the gate field.

The properties mentioned above are quite intriguing, as they enable us to create a model for gate controlling efficiency, denoted as $V_{\mathrm{G}}^{\mathrm{eff(M)}}(V_g)$. This model is based on the slopes of $eV_{\mathrm{G}}^{\mathrm{eff(N)}}(V_g)$, denoted as $\alpha_{\mathrm{in}} \approx 0.83$ and $\alpha_{\mathrm{out}} \approx 0.33$. In the Pt–$WSe_2$–Pt FET without h-AlN, the chemical potential is positioned outside the band gap at $V_{\mathrm{g}}=0$. Taking the transmission function $\tau(E; V_{\mathrm{g}}=0)$ as the baseline, the model for the effective gate voltage, $V_{\mathrm{G}}^{\mathrm{eff(M)}}$, is as follows:

$$V_{\mathrm{G}}^{\mathrm{eff(M)}}(V_g) = \begin{cases} \alpha_{\mathrm{out}} V_g, & \text{for } V_g < \frac{E_{\mathrm{V0}}}{e} \\ \alpha_{\mathrm{in}} V_g + \frac{(\alpha_{\mathrm{out}}-\alpha_{\mathrm{in}})E_{\mathrm{V0}}}{e}, & \text{for } \frac{E_{\mathrm{V0}}}{e} \le V_g \le \frac{E_{\mathrm{C0}}}{e} \\ \alpha_{\mathrm{out}} V_g + \frac{(\alpha_{\mathrm{in}}-\alpha_{\mathrm{out}})(E_{\mathrm{C0}}-E_{\mathrm{V0}})}{e}, & \text{for } V_g > \frac{E_{\mathrm{C0}}}{e} \end{cases} \tag{12}$$

where $E_{\mathrm{V0}} \equiv [E_{\mathrm{V}}(V_{\mathrm{g}}=0)-\mu]/\alpha_{\mathrm{out}}$ and $E_{\mathrm{C0}} \equiv E_{\mathrm{V0}} + [E_{\mathrm{C}}(V_{\mathrm{g}}=0)-E_{\mathrm{V}}(V_{\mathrm{g}}=0)]/\alpha_{\mathrm{in}}$.

Similarly in the Pt–WSe_2–Pt FET with h-AlN, the chemical potential is positioned within the band gap. The model for the effective gate voltage, $V_{\mathrm{G}}^{\mathrm{eff(M)}}$, is as follows: taking the transmission function $\tau(E; V_{\mathrm{g}}=0)$ as the baseline, the model for the effective gate voltage, $V_{\mathrm{G}}^{\mathrm{eff(M)}}$, is as follows:

$$V_{\mathrm{G}}^{\mathrm{eff(M)}}(V_g) = \begin{cases} \alpha_{\mathrm{out}} V_g + \frac{(\alpha_{\mathrm{in}}-\alpha_{\mathrm{out}})E_{\mathrm{V0}}}{e}, & \text{for } V_g < \frac{E_{\mathrm{V0}}}{e} \\ \alpha_{\mathrm{in}} V_g, & \text{for } \frac{E_{\mathrm{V0}}}{e} \le V_g \le \frac{E_{\mathrm{C0}}}{e} \\ \alpha_{\mathrm{out}} V_g + \frac{(\alpha_{\mathrm{in}}-\alpha_{\mathrm{out}})E_{\mathrm{C0}}}{e}, & \text{for } V_g > \frac{E_{\mathrm{C0}}}{e}, \end{cases} \tag{13}$$

where $E_{\mathrm{V0}} \equiv [E_{\mathrm{V}}(V_{\mathrm{g}}=0)-\mu]/\alpha_{\mathrm{in}}$ and $E_{\mathrm{C0}} \equiv [E_{\mathrm{C}}(V_{\mathrm{g}}=0)-\mu]/\alpha_{\mathrm{in}}$.

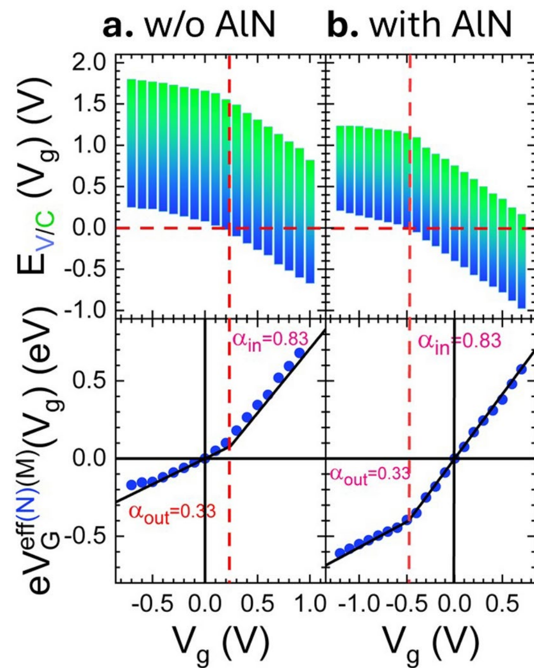

Fig. 6. Position of Band gap and V_G^{eff} shifted by V_g. The top panels of (**a**) and (**b**) illustrate the displacement of the band gaps due to the V_g for the Pt–WSe_2–Pt (**a**) without and (**b**) with h-AlN in the gate structures for the Pt–WSe_2–Pt (**a**) without and (**b**) with the insertion of h-AlN single layers in the gate structures. The horizonal red-dashed line represents the chemical potential μ of the right lead at $V_g = 0$. The gate voltages V_g, which can shift the band gap's $E_V(V_g)$ to $\mu = 0$, are indicated by the vertical red-dashed line; The bottom panels of (**a**) and (**b**) represent $eV_G^{eff(N)} \equiv E_V(V_g) - E_V(V_g = 0)$ (blue solid circles) and $eV_G^{eff(N)}$ (black solid lines) as a function of V_g. The slopes α_{in} and α_{out} determine the gate controlling effciciency when the chemical potential is inside

Pt–WSe_2–Pt	α_{in}	α_{out}	E_{V0} (eV)	E_{C0} (eV)
w/o h-AlN	0.83	0.33	0.88	2.13
with h-AlN	0.83	0.33	-0.43	0.27

Table 1. Parameters for the model effective gate voltage, $V_G^{eff(M)}(V_g)$, in the Pt–WSe_2–Pt FET without and with h-AlN.

In the bottom panels of Fig. 6a,b, the model effective gate voltage, $V_G^{eff(M)}(V_g)$, is displayed as black solid lines as a function of V_g for the Pt–WSe_2–Pt FETs, respectively, with and without h-AlN. Taking the transmission function $\tau(E; V_g = 0)$ as the baseline, the applied gate voltage, V_g, will shift the chemical potential from $\mu = 0$ at $V_g = 0$ to $[\mu + eV_G^{eff(N\ or\ M)}(V_g)]$ at V_g. This property is illustrated in the bottom panel of Fig. 5a,b, where the energy shift of the chemical potential is $[eV_G^{eff(N\ or\ M)}(V_g)]$ (the horizontal axis) due to the application of V_g (the vertical axis). Table 1 lists the parameters for $V_G^{eff(M)}(V_g)$ for FETs without and with the h-AlN.

We compare J_N and J_M for the Pt–WSe_2–Pt FETs (a) without and (b) with h-AlN in the gate structures with the same equivalent oxide thickness (EOT), as can be seen in the top panels of Fig. 7a,b. The current density $J_N(V_g)$ is computed self-consistently from first-principles calculations for each gate voltage V_g using Nanodcal [c.f. Eq. (3)] in contrast to $J_M[V_G^{eff(M)}(V_g)]$ is calculated using the model effective gate voltage $V_G^{eff(M)}(V_g)$ and the transmission function $\tau(E; V_g = 0)$ at $V_g = 0$ [c.f. Eqs. (7)–(9)]. We also compare S.S.(N) and S.S.(M) referring the right axis, where S.S.(N) is the subthreshold swing calculated from J_N, while S.S.(M) is the subthreshold swing computed from J_M. We assume that the FETs are operating in the V_g range of 0.7 V. The FET without AlN shows properties of P-type transistor. The on-current density J_{On} for is approximately 763 μA/μm at $V_g = 0$ V, and the off-current density J_{Off} is approximately 3×10^{-4} μA/μm at $V_g = 0.7$ V.The on/off ratio is roughly 2.5×10^6, and the subthreshold swing ranges from 73 to 586 mV/dec. The FET with AlN displays properties of bipolar transistor. The on-current density J_{On} for is approximately 677 μA/μm at $V_g = -0.7$ V, and the off-current density J_{Off} is approximately 4×10^{-4} μA/μm at $V_g = 0$ V. The on/off ratio is roughly 1.7×10^6, and the subthreshold swing ranges from 70 to 581 mV/dec. A list of the FET specifications is summarized in Table 2.

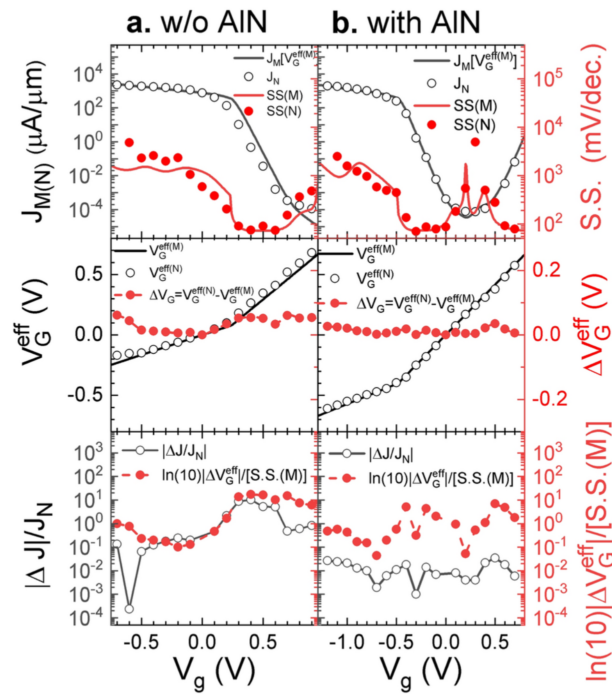

Fig. 7. Comparison of J_N and J_M, and the relative error between them. The top panels of (**a**) and (**b**) compare J_M (black solid line) with J_N (black open circles) referring to the left axis, and the subthreshold swings S.S (M) (red solid line) with S.S. (N) (red solid circles) referring to the right axis as a function of V_g; The middle panels of (**a**) and (**b**) compare $V_G^{eff(M)}(V_g)$ (black solid line) with $V_G^{eff(N)}(V_g)$ (black open circles) referring to the left axis, and their difference $\Delta V_G(V_g)^{eff}$ (red solid circles) referring to the right axis as a function of V_g; The

Pt–WSe_2–Pt	J_{On}	$V_g(On)$	J_{Off}	$V_g(Off)$	on/off ratio	S.S.
w/o h-AlN	763	0	3×10^{-4}	-0.7	2.5×10^6	73–586
w/h-AlN	677	0.7	4×10^{-4}	0	1.7×10^6	69–581

Table 2. Specifications of the Pt–WSe_2–Pt FETs with the gate voltage V_g operating in the range of 0.7 V.

Equation (11) can be used to estimate the relative error between the current density computed from first-principles and the approximation current density computed from the model gate voltage. In Fig. 7a,b, the middle panels show ΔV_G^{eff} for the FETs without AlN and with AlN, with reference to the right axis. The bottom panels compare $\left|\frac{\Delta J}{J_N}\right|$ with $[ln(10)\left|\Delta V_G^{eff}\right|/S.S.]$ for the FETs without AlN and with AlN. It is demonstrated that the relative error between J_N and J_M falls within $[ln(10)\left|\Delta V_G^{eff}\right|/S.S.]$, where the subthreshold swing is chosen as S.S.(M) calculated from J_M.

Conclusions

Motivated by recent advances in the growth of h-AlN via ALD on TMD monolayes by C. M. Hu's group, we conduct first-principles calculations to investigate the device performance of Pt–WSe_2–Pt FETs without and with the inclusion of h-AlN monolayer as a spacer in the gate architecture. The task was completed using Nanodcal, a combination of density functional theory and non-equilibrium Green's function. When AlN is epitaxially grown on TMD layers, the crystal structure of AlN undergoes a transition from the three-dimensional Wurtzite structure to a two-dimensional h-AlN structure. We examined the electronic configurations of h-AlN layers deposited on top of a WSe_2 monolayer to assess the stability of the structure. We accomplished the task by using VASP, which is based on density functional theory. In further, we compute the transmission functions $[\tau(E; V_g)]$ and current density $[J_N(V_g)]$ as a function of gate voltages V_g at $V_{ds} = 50$ mV. We compared $\tau(E; V_g)$ and $J_N(V_g)$ of Pt–WSe_2 2–Pt FETs with and without h-AlN monolayers. We discovered that adding h-AlN can change the transistor's characteristics. The Pt–WSe_2–Pt nanojunctions exhibited excellent FET deivice characteristics. The FET without h-AlN exhibits the characteristics of a P-type transistor, with an on/off ratio of around 2.5×10^6, and an average subthreshold swing of approximately 109 mV/$\mathrm{dec.}$ In contrast, the FET with AlN exhibits the characteristics of a bipolar transistor, with an on/off ratio of around 1.7×10^6, and an average S.S. of approximately 112 mV/$\mathrm{dec.}$ We

observed that the application of V_g shifts $\tau(E;V_g)$ by an energy of $\alpha(eV_g)$. The gate-controlling efficiencies (α) are $\alpha_{in}=83\%$ if the Fermi energy position is inside the energy gap, and $\alpha_{out}=33\%$ if it is outside the energy gap. This observation allows us to construct an effective gate model [$V_G^{eff(N)}$] based on the Landauer formula, with the baseline $\tau(E;V_g=0)$. For current densities, the relative error between model and first-principles calculations is less than $[\frac{ln(10)}{S.S.}]|\Delta V_G^{eff}|$. The effective gate model [$V_{G^{eff(M)}}$] combined with the Landauer formula provides an efficient way to compute the current density and can save a lot of computing power compared to first-principles calculations using Nanodcal. The results of our research could be valuable for advancing the design of FETs based on TMD materials.

Data availability

All data included in this study are available upon request by contact with the corresponding author, Yu-Chang Chen (yuchangchen@nycu.edu.tw).

Received: 11 June 2024; Accepted: 27 September 2024
Published online: 14 October 2024

References

1. Akinwande, D. et al. Graphene and two-dimensional materials for silicon technology. *Nature* **573**, 507 (2019).
2. Liu, Y. et al. Promises and prospects of two-dimensional transistors. *Nature* **591**, 43 (2021).
3. Yoon, Y., Ganapathiand, K. & Salahuddin, S. How good can monolayer mos2 transistors be?. *Nano Lett.* **11**, 3768 (2011).
4. Popov, I., Seifert, G. & Tománek, D. Designing electrical contacts to mos2 monolayers: A computational study. *Phys. Rev. Lett.* **108**, 156802 (2012).
5. Das, S., Chen, H.-Y., Penumatcha, A. V. & Appenzeller, J. High performance multilayer mos2 transistors with scandium contacts. *Nano Lett.* **13**, 100 (2013).
6. Kang, J., Liu, W. & Banerjee, K. High-performance mos2 transistors with low-resistance molybdenum contacts. *Appl. Phys. Lett.* **104**, 093106 (2014).
7. Kang, J., Liu, W., Sarkar, D., Jena, D. & Banerjee, K. Computational study of metal contacts to monolayer transition-metal dichalcogenide semiconductors. *Phys. Rev. X* **4**, 031005 (2014).
8. Nayak, A. P. et al. Pressure-induced semiconducting to metallic transition in multilayered molybdenum disulphide. *Nat. Commun.* **5**, 3731 (2014).
9. Zhu, J. et al. Argon plasma induced phase transition in monolayer mos2. *J. Am. Chem. Soc.* **139**, 10216 (2017).
10. Lin, Y.-C., Dumcenco, D. O., Huang, Y.-S. & Suenaga, K. Atomic mechanism of the semiconducting-to-metallic phase transition in single-layered mos2. *Nat. Nanotech.* **9**, 391 (2014).
11. Cho, S. et al. Phase patterning for ohmic homojunction contact in mote2. *Science* **349**, 625 (2015).
12. Jiang, J. et al. Yttrium-induced phase-transition technology for forming perfect ohmic contact in two-dimensional mos2 transistors. *Res. Square*. (2023).
13. Kappera, R. et al. Phase-engineered low-resistance contacts for ultrathin mos2 transistors. *Nat. Mater.* **13**, 1128 (2014).
14. Villaos, R. A. B. et al. Thickness dependent electronic properties of pt dichalcogenides. *NPJ 2D Mater. Appl.* **3**, 2 (2019).
15. Li, J. et al. Layer-dependent band gaps of platinum dichalcogenides. *ACS Nano* **15**, 13249 (2021).
16. AlMutairi, A., Yin, D. & Yoon, Y. Ptse2 field-effect transistors: New opportunities for electronic devices. *IEEE Electron Device Lett.* **39**, 151 (2018).
17. Yang, E., Seo, J. E., Seo, D. & Chang, J. Intrinsic limit of contact resistance in the lateral heterostructure of metallic and semiconducting ptse2. *Nanoscale* **12**, 14636 (2020).
18. Shen, P.-C. et al. Ultralow contact resistance between semimetal and monolayer semiconductors. *Nature* **593**, 211–217 (2021).
19. Chou, A.-S. et al. Antimony semimetal contact with enhanced thermal stability for high performance 2d electronics. *2021 IEEE International Electron Devices Meeting (IEDM)* pp. 7.2.1–7.2.4 (2021).
20. Qu, H., Zhang, S. & Zeng, H. Two-dimensional $\mathrm{MS}\,\mathrm{i}_2\,\mathrm{N}_4$ heterostructure p-type transistors with sub-thermionic transport performances. *IEEE Electron Device Lett.* **44**, 1492–1495 (2023).
21. Qu, H. et al. Identifying atomically thin isolated-band channels for intrinsic steep-slope transistors by high-throughput study. *Sci. Bull.* **69**, 1427–1436 (2024).
22. Fang, H. et al. High-performance single layered wse2 p-fets with chemically doped contacts. *Nano Lett.* **12**, 3788 (2012).
23. Tosun, M. et al. Air-stable n-doping of wse2 by anion vacancy formation with mild plasma treatment. *ACS Nano* **10**, 6853 (2016).
24. Jiang, J. et al. A facile and effective method for patching sulfur vacancies of ws2 via nitrogen plasma treatment. *Small* **15**, 1901791 (2019).
25. Chung, C.-H., Chen, H.-R., Ho, M.-J. & Lin, C.-Y. Ws2 transistors with sulfur atoms being replaced at the interface: First-principles quantum-transport study. *ACS Omega* **8**, 10419 (2023).
26. Iqbal, M. W. et al. High-mobility and air-stable single-layer ws2 field-effect transistors sandwiched between chemical vapor deposition-grown hexagonal bn films. *Sci. Rep.* **5**, 10699 (2015).
27. Chang, S.-J. et al. van der waals epitaxy of 2d h-aln on tmds by atomic layer deposition at 250 Â°c. *Appl. Phys. Lett.* **120**, 162102 (2022).
28. Hohenberg, P. & Kohn, W. Inhomogeneous electron gas. *Phys. Rev.* **136**, B864 (1964).
29. Kohn, W. & Sham, L. J. Self-consistent equations including exchange and correlation effects. *Phys. Rev.* **140**, A1133 (1965).
30. Levy, M. Universal variational functionals of electron densities, first-order density matrices, and natural spin-orbitals and solution of the v-representability problem. *Proc. Natl. Acad. Sci. USA* **76**, 6062 (1979).
31. Perdew, J. P., Burke, K. & Ernzerhof, M. Generalized gradient approximation made simple. *Phys. Rev. Lett.* **78**, 3865 (1997).
32. Kresse, G. & Hafner, J. Ab initio molecular dynamics for liquid metals. *Phys. Rev. B* **47**, 558(R) (1993).
33. Kresse, G. & Furthmüller, J. Efficient iterative schemes for ab initio total-energy calculations using a plane-wave basis set. *Phys. Rev. B* **54**, 11169 (1996).
34. Kresse, G. & Furthmüller, J. Efficiency of ab-initio total energy calculations for metals and semiconductors using a plane-wave basis set. *Comput. Mater. Sci.* **6**, 15 (1996).
35. Kresse, G. & Joubert, D. From ultrasoft pseudopotentials to the projector augmented-wave method. *Phys. Rev. B* **59**, 1758 (1999).
36. Taylor, J., Guo, H. & Wang, J. Ab initio modeling of quantum transport properties of molecular electronic devices. *Phys. Rev. B* **63**, 245407 (2001).
37. Waldron, D., Haney, P., Larade, B., MacDonald, A. & Guo, H. Nonlinear spin current and magnetoresistance of molecular tunnel junctions. *Phys. Rev. Lett.* **96**, 166804 (2006).
38. Keldysh, L. V. Diagram technique for nonequilibrium processes. *Sov. Phys. JETP.* **20**, 1018 (1965).
39. Datta, S. *Electron Transport in Mesoscopic Systems* (Cambridge University Press, 1995).

40. Economou, E. N. *Green's Function in Quantum Physics*, 3rd Edn. (Springer, 2006).
41. Troullier, N. & Martins, J. L. Efficient pseudopotentials for plane-wave calculations. *Phys. Rev. B* **43**, 1993 (1991).
42. Perdew, J. P. et al. Atoms, molecules, solids, and surfaces: Applications of the generalized gradient approximation for exchange and correlation. *Phys. Rev. B* **46**, 6671 (1992).
43. Gusakova, J. et al. Electronic properties of bulk and monolayer tmds: Theoretical study within dft framework (gvj-2e method). *Phys. Status Solidi A* **214**, 1700218 (2017).
44. Hulliger, F. *Structural Chemistry of Layer-Type Phases* (Springer, 1976).
45. Patoary, N. H. et al. Improvements in 2d p-type wse2 transistors towards ultimate cmos scaling. *Sci. Rep.* **13**, 3304 (2023).
46. Grimme, S. Semiempirical gga-type density functional constructed with a long-range dispersion correction. *J. Comput. Chem.* **27**, 1787 (2006).
47. Landauer, R. Spatial variation of currents and fields due to localized scatterers in metallic conduction. *IBM J. Res. Develop.* **1**, 223 (1957).
48. Büttiker, M., Imry, Y., Landauer, R. & Pinhas, S. Generalized many-channel conductance formula with application to small rings. *Phys. Rev. B* **31**, 6207 (1985).
49. Büttiker, M. Four-terminal phase-coherent conductance. *Phys. Rev. Lett.* **57**, 1761 (1986).
50. Grosso, G. & Parravicini, G. P. *Solid State Physics* (Academic Press, 2000).

Acknowledgements

This work was financially supported by NCS (Taiwan) for support under Grant NSTC 111-2112-M-A49-032, and the "Advanced Semiconductor Technology Research Center" from The Featured Areas Research Center Program within the framework of the Higher Education Sprout Project by the Ministry of Education (MOE) in Taiwan. Also supported in part by the National Science and Technology Council, Taiwan, under Grant No. NSTC 111-2634-F-A49-008. We thank to National Center for High-performance Computing (NCHC) for providing computational and storage resources. We express our gratitude to the CTCP, NYCU, Taiwan for their support. We wish to express our gratitude for the guidance provided by Professor Chenming Calvin Hu, and useful discussion with Professor Chiung-Yuan (Gene) Lin, and Professor Chao-Cheng Kaun.

Additional information

Correspondence and requests for materials should be addressed to Y.-C.C.

Reprints and permissions information is available at www.nature.com/reprints.

Publisher's note Springer Nature remains neutral with regard to jurisdictional claims in published maps and institutional affiliations.

Open Access This article is licensed under a Creative Commons Attribution-NonCommercial-NoDerivatives 4.0 International License, which permits any non-commercial use, sharing, distribution and reproduction in any medium or format, as long as you give appropriate credit to the original author(s) and the source, provide a link to the Creative Commons licence, and indicate if you modified the licensed material. You do not have permission under this licence to share adapted material derived from this article or parts of it. The images or other third party material in this article are included in the article's Creative Commons licence, unless indicated otherwise in a credit line to the material. If material is not included in the article's Creative Commons licence and your intended use is not permitted by statutory regulation or exceeds the permitted use, you will need to obtain permission directly from the copyright holder. To view a copy of this licence, visit http://creativecommons.org/licenses/by-nc-nd/4.0/.

© The Author(s) 2024